Sensors and Actuators B 150 (2010) 556–563

Contents lists available at ScienceDirect

Sensors and Actuators B: Chemical

journal homepage: www.elsevier.com/locate/snb

Design and fabrication of porous polymer wick structures

Viktor Shkolnikov[1], Daniel G. Strickland[2], David P. Fenning[3], Juan G. Santiago*

Department of Mechanical Engineering, Stanford University, Stanford, CA 94305, USA

ARTICLE INFO

Article history:
Received 4 May 2010
Received in revised form 17 August 2010
Accepted 26 August 2010
Available online 28 September 2010

Keywords:
Wick
Porous polymer monolith
Capillary transport
In situ polymerization
Carman–Kozeny
Permeability

ABSTRACT

Wicks are often an integral part of fluid capacitance and transport in many systems, including heat pipes, fuel cells, and lateral flow chemical assays on cellulose paper. In this paper, we explore porous polymer monoliths as a new wick material potentially applicable to these and other applications. Polymer monolith chemistries, long used for high surface-to-volume ratio separation and filtering media in analytical chemistry, offer tremendous flexibility in resulting monolith pore structure, chemical composition, and surface chemistry (including wettability). We leverage this flexibility to design, fabricate, and characterize hydrophilic porous monoliths, with the aim of achieving high permeability wick materials. We show that variations in monomer concentration and porogen composition can affect mode pore diameters ranging from 6.3 to 10.1 μm and permeabilities ranging from 0.73×10^{-12} to 1.9×10^{-12} m^2. In addition, we identify a rough dependence of monolith permeability on porosity times the square of mode pore diameter and discuss key figures of merit characterizing capillary transport. As an example application, we then detail a custom injection molding procedure, where we *in situ* polymerize ~150 μm thick wicks conformally onto the surface of metal channels of a polymer electrolyte fuel cell cathode.

1. Introduction

In 1990, Tennikova et al. [1] first demonstrated highly cross-linked, rigid, microporous polymer monoliths as separation media for high performance membrane chromatography. This initial demonstration has since led to a wide variety of techniques for preparation of porous polymer monoliths, which allow control over pore morphology, mechanical stability, and surface chemistry [2]. Pore size distributions are often bimodal, with large and small pores resulting in materials with both high permeability and high specific surface area. These materials are therefore ideal for many separation applications including liquid chromatography [3], capillary separations [4], capillary electrochromotography [5–7], thin layer chromatography [8] and, more recently, gas chromatography [9]. In addition, polymer monoliths have been used as porous frits in electroosmotic pumps [10], in microfluidic devices for on-chip separations and low Reynolds number mixing [11,12], as hydrogen storage media [13], and for water management in fuel cells [14]. To our knowledge, outside of the recent effort by Strickland and Santiago [14], there have been no dedicated efforts aimed at realizing high permeability, hydrophilic, porous polymer monoliths suitable for wicking and other liquid transport applications.

Porous polymer monoliths are synthesized by carrying out free-radical polymerization of cross-linking and monovinyl monomers, in the presence of solvents. Heat, ultraviolet (UV) irradiation, or gamma-rays generate free radicals by destabilizing an initiating compound [2]. These free radicals initiate rapid polymer chain growth at what become nucleation sites, which continue to grow as the reaction proceeds. As polymer molecular weight increases, solubility decreases, and a two-phase system of solid polymer and liquid solvent results. The resulting monolith microstructure consists of an agglomeration of globules, whose size directly impacts resulting pore size distribution. Globule size is influenced by many factors, including the number of nucleation sites present, monomer concentration, solubility, and degree of cross-linking [15]. Thus, polymer microstructure can be controlled by rate of reaction, monomer/porogen ratio, type of porogenic solvents and fraction of cross-linking monomers. Detailed descriptions of various chemistries and characterization of resulting monoliths can be found in [2,15].

In the present work, we designed, fabricated, and characterized porous monoliths of 2-hydroxyethyl methacrylate-*co*-ethylene dimethacrylate (HEMA-*co*-EDMA) with the aim of achieving high permeability, hydrophilic, dimensionally and chemically stable materials for use as wicks. In general, wicks are porous, hydrophilic structures that are commonly used to absorb and transport liquids. Wicks are applied to heat pipes and vapor chambers [16],

* Corresponding author. Tel.: +1 650 723 7657; fax: +1 650 723 5689.
E-mail address: juan.santiago@stanford.edu (J.G. Santiago).
[1] Co-first author.
[2] Co-first author, now at Santa Clara University.
[3] Now at Massachusetts Institute of Technology.

0925-4005/$ – see front matter © 2010 Elsevier B.V. All rights reserved.
doi:10.1016/j.snb.2010.08.040

microfluidic systems [17], lateral flow chemical assays on cellulose paper [18], fuel cells [19,20], and electrospray nozzles [21]. For most applications, an ideal wick has high permeability and can support significant capillary-pressure-induced liquid pressure gradients. Often these two properties are in competition: large pores are required for high permeability, while small pores induce large capillary pressures. In the following sections, we identify key parameters affecting resulting monolith permeability and pore size, discuss competing microstructure properties in detail, and identify strategies to optimize performance for a given application. As an example application, we then discuss a custom injection molding procedure, where we integrated wicks with order 100 μm feature sizes in a polymer electrolyte fuel cell cathode flow field. The latter integration was described as part of a prototype fuel cell system we reported previously [14], however, that study centered on the performance of the wick as a component of the system. Here, we present new analysis, methods, and results which specifically focus on the chemistry, process optimization, molding, *in situ* polymerization, and capillary transport properties of the wick structure itself. Our aim is to enable wider applications of such *in situ* polymerized wicks.

2. Materials and methods

We here describe materials, discuss choice of chemistry, and present *ex situ* fabrication methods of polymer monolith samples used for characterization. Characterization included permeability, pore size, and surface area measurements. We describe *in situ* polymerization of the monolith structures in Section 4.

2.1. Materials

Ethylene dimethacrylate (EDMA – CAS# 97-90-5), 2-hydroxyethyl methacrylate (HEMA – CAS# 868-77-9), inhibitor removal media (product number: 311332 – CAS# 9003-70-7), benzoin methyl ether (CAS# 3524-62-7), and methanol (MeOH) 99.93% were purchased from Aldrich. n-Hexane HPLC grade 95+% was purchased from Alfa Aesar. GE Type 214 quartz tubing (5 mm i.d., 7 mm o.d.) was purchased from National Scientific Company Inc. (Quakertown, PA). GE Type 214 quartz tubing was chosen for its high (>90%) UV 360 nm wavelength transmittance [22].

2.2. Polymer chemistry

Wicking structures require hydrophilic surface functionality to absorb water or aqueous solutions. We therefore chose a polymerization chemistry that incorporates the monovinyl monomer, HEMA, which has a polar hydroxyl functional group. Adapting a chemistry from Yu et al. [23], we cross-linked HEMA with EDMA via free radical, UV-initiated polymerization in the presence of MeOH and hexane as solvents. As Yu et al. showed, an MeOH/Hexane binary solvent system provides satisfactory solubility for polymerization and is ideal for large-pore formation (we discuss effect of polymer solubility on pore size in Section 3.1.3).

We photo-initiated polymerization via UV irradiation and destabilization of benzoin methyl ether. We chose photo, rather than thermal, initiation for the present polymerization. Thermal initiators often require long polymerization times and elevated temperatures, which can lead to significant evaporative loss of solvents in imperfectly sealed molds. In contrast, photo-initiation can be carried out at room temperature over shorter polymerization times, thus minimizing evaporative solvent loss.

To characterize the chemistry and resulting monoliths, we varied two separate ratios: (1) total monomer/solvent and (2) MeOH/hexane. We list recipes in Table 1. In all cases, 1.25% (by mass, with respect to monomers) benzoin methyl ether was used.

2.3. Fabrication of samples for ex situ permeability and pore size measurements

Both EDMA and HEMA were received with polymerization inhibitors, which we removed by passing through columns packed with inhibitor removing media. We then mixed the photo-initiator (benzoin methyl ether), HEMA, EDMA, MeOH and hexane in the order listed, in glass vials and subsequently purged with nitrogen to minimize oxygen dissolved in solution. Purge was carried out by bubbling nitrogen at 3×10^{-9} m^3 s^{-1} for ~2.5 min. In all cases, solution weight change before and after purge was less than 3%.

We transferred solutions into quartz tubes, which we sealed with custom-fabricated Teflon caps. We then irradiated samples using a 100 W, ~365 nm peak wavelength UV lamp, at 8 cm exposure distance, for 1 h. During polymerization, solution changed from transparent to white and visibly opaque in less than 10 min. After polymerization, we flushed samples with methanol to remove unreacted monomers and solvents, and dried at 120 °C for 1 h.

Table 1
Tested properties of porous polymer monolith.

Name	Chemical composition[a]				Properties								
	HEMA	EDMA	MeOH	Hex	ε[b]	d_{mode}[c]	d_{median}[d]	σ[e]	V_{pore}[f]	s_o[g]	k[h]	$d_{p,eq}$[i]	k/d_{mode}[j]
HE04	0.15	0.15	0.28	0.42	0.77	8.6	7.6	1.1	3.0	58.7	1.31	36.5	0.15
HE05	0.15	0.15	0.35	0.35	0.77	10.1	7.2	2.4	4.6	75.0	1.53	39.3	0.15
HE06	0.15	0.15	0.42	0.28	0.77	9.0	8.4	0.93	3.6	61.7	1.91	44.0	0.21
HE13	0.20	0.20	0.24	0.36	0.68	7.6	6.8	1.1	2.6	36.1	0.942	30.9	0.12
HE14	0.20	0.20	0.30	0.30	0.68	7.9	6.8	1.6	2.5	35.6	1.18	34.6	0.15
HE15	0.20	0.20	0.36	0.24	n/a	n/a	n/a	n/a	n/a	n/a	n/a	n/a	n/a
HE22	0.25	0.25	0.20	0.30	0.59	6.3	3.3	1.8	2.1	37.5	0.726	27.1	0.12
HE23	0.25	0.25	0.25	0.25	n/a	n/a	n/a	n/a	n/a	n/a	n/a	n/a	n/a
HE24	0.25	0.25	0.30	0.30	n/a	n/a	n/a	n/a	n/a	n/a	n/a	n/a	n/a

[a] Concentration by mass fraction (g g^{-1})
[b] Porosity, taken as volume fraction of monomers.
[c] Most common pore diameter, taken as peak of pore size distribution (μm).
[d] Median pore diameter, taken as pore size at 50% of total pore volume during mercury intrusion (μm).
[e] Characteristic pore size distribution width (μm).
[f] Pore volume (mL g^{-1}).
[g] Specific surface area (m^2 g^{-1}).
[h] Permeability ($\times 10^{-12}$ m^2).
[i] Equivalent particle diameter (μm).
[j] Capillary transport parameter (μm).

2.4. Measurement of permeability

Permeability, k, of a specific porous material can be interpreted as a material property. Specifically, it is the proportionality constant in Darcy's law relating pressure gradient to superficial fluid velocity in porous media [24]. A form of Darcy's law is:

$$\vec{u} = \frac{k}{\mu}\nabla P_l, \quad (1)$$

where μ is fluid viscosity, $\vec{u}$ is the superficial liquid velocity, and ∇P_l is the pressure gradient in the liquid phase. $\vec{u}$ can be integrated over the cross-sectional area normal to the flow to obtain a linear relationship between pressure gradient and flow rate. Assuming a one dimensional linear pressure distribution and rearranging, this yields $k = \mu(Q/\Delta P)(L/A)$, where Q is the flow rate, A is the cross-sectional area normal to the superficial velocity vector, and L is the distance across which the pressure difference, ΔP, is applied. To measure permeability, we manually pushed the samples out of the quartz tubing and transferred them into 3/16″ heat shrink tubing (SPC Technology, Chicago, IL). Heat shrink is thin-walled polymer tubing which, upon heating, permanently contracts and can conform to shapes inside it. Heat shrink sealed around and connected samples to silicone tubes on either end. We observed a good seal around polymer samples with minimal dimensional change due to compression.

We connected samples to a mass flow controller (MC-5SLPM-D, Alicat Scientific, Tucson, AZ) and upstream pressure transducer (PX139 – 030D4V Omega Engineering, Stamford, CT). Permeability was measured by flowing air (ultra zero grade compressed air cylinder, Praxair Inc., San Ramon, CA) through the sample at seven different flow rates in the range of 20–1000 sccm. We set flow rate and measured ΔP across the sample using a PC with LabView 8.5. To determine k, we performed a linear regression fit for each sample to determine the $Q/\Delta P$ slope. R^2 values for these fits were higher than 0.98, indicating relatively constant permeability over the range tested. Since ΔP depends linearly on Q, we determined permeability by directly substituting $Q/\Delta P$ into the above derived one dimensional expression for k. We report results in Table 1.

3. Results

The microstructure of a porous wick material strongly affects its capacity to transport fluids. In this section, we first discuss mechanisms and general trends in resulting monolith microstructure. We then explore the corresponding impact on monolith permeability and capillary transport. Finally, we detail a method for integrating wick structures into a fuel cell as a sample application which requires fine geometric control.

3.1. Review of general mechanisms and trends in monolith polymerization

Mechanisms and trends for methacrylate monolith polymerization chemistries are discussed in detail by Vlakh et al. [25]. We summarize here major concepts from Vlakh et al. as we leveraged their study to guide our design and characterization experiments. As mentioned above, four main parameters control resulting monolith structure and properties: (1) rate of reaction, (2) monomer/porogen ratio, (3) solubility and (4) degree of cross-linking.

3.1.1. Rate of reaction

Typically, photo- or thermal initiators are used to induce polymerization. Initiators form free radicals when exposed to UV radiation or heat, which then induce rapid polymer chain growth by opening and linking monomer vinyl groups. As such, initiator concentration, reaction temperature, and irradiation intensity all influence reaction rate. In general, characteristic pore size decreases with increasing reaction rate. This relationship is attributed to increased polymer nucleation site concentration, which affects polymer globules of increased number density and smaller characteristic dimension.

3.1.2. Monomer-to-porogen ratio

Porosity is roughly equal to the volumetric fraction of porogenic solvents present [26]. The volumetric ratio of total monomer to total porogenic solvent, therefore, gives fairly direct control over resulting monolith porosity. Physical properties of resulting monoliths limit the range of porosities that can be achieved: non-porous samples typically result at high monomer concentration (roughly >0.6 mL mL^{-1}), while samples become friable for low monomer concentration (<0.2 mL mL^{-1}).

3.1.3. Solubility

A binary solvent system, comprised of a good and poor solvent, is typically used to control polymer solubility. In general, pore size increases with decreasing solubility of monomers. When a poor solvent is used, polymers become insoluble at lower molecular weights and therefore precipitate early in the reaction. Remaining monomers are a better solvent than the poor solvent selected, resulting in increased monomer concentration in their vicinity. Polymer growth near existing globules is therefore thermodynamically preferred, and leads to fewer polymer globules of larger characteristic dimension.

3.1.4. Degree of cross-linking

Degree of cross-linking is controlled by the ratio of multi-vinyl to monovinyl monomers. Changing this ratio affects both the pore size distribution and the chemical composition of the resulting polymer monolith. Pore size typically decreases as degree of cross-linking increases. During reaction, highly cross-linked polymers quickly become insoluble. This results in increased globule number density, and associated polymer globules of smaller characteristic dimension.

3.2. Control and optimization of wick porosity and pore structure

We limited the present study to exploring the effect of monomer/porogen ratio and solubility on resulting monolith pore structure when using HEMA and EDMA as monomers. We refer the reader to work by Yu et al. [23] for characterization of a similar hydrophilic chemistry and comparison of resulting microstructure with additional EDMA cross-linked porous polymers (including those with hydrophobic surface chemistry). The data shown here represents example trends in synthesizing monoliths as part of a 3×3 parametric study, where we varied both monomer/solvent ratio and solubility (via the binary solvent mixture). We fabricated and characterized monoliths for monomer/solvent ratios of 30/70, 40/60, and 50/50, and MeOH/hexane ratios of 40/60, 50/50, and 60/40 (by mass). In all cases, HEMA/EDMA ratio was 50/50. Resulting monoliths were characterized using mercury intrusion porosimetry to determine pore size distribution and BET analysis to measure specific surface area (Porous Materials, Inc., Ithaca, NY). We measured monolith permeability in-house, as described in Section 2.4. Table 1 summarizes results. Chemistries for which resulting monoliths were non-porous are indicated with an "n/a" in the porous properties entries.

In Fig. 1, we plot mode pore diameter versus the gravimetric fractions $w_{MeOH} = m_{MeOH}/m_{solvents}$ and $w_{solvent} = m_{solvents}/m_{total}$. Note, we use here the term "mode pore diameter" to describe the characteristic scale of the pores of the monoliths, which we take

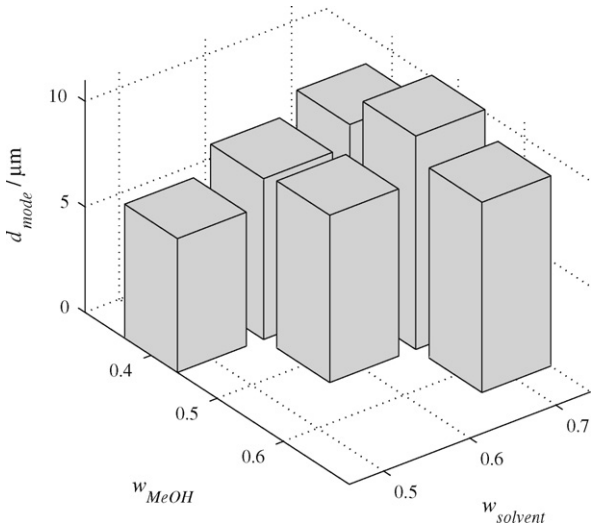

Fig. 1. Mode pore diameter as a function of mass fractions w_{MEOH} (=$m_{MeOH}/m_{solvents}$) and $w_{solvent}$ (=$m_{solvents}/m_{total}$). Mode pore diameter roughly increases with both increasing solvent and MeOH fractions. Pore diameter dependence on solvent fraction is more pronounced.

as the peak of the pore size distribution determined from mercury intrusion porosimetry measurements. We recognize that monolith morphology is complex and pores are not cylindrical (circular cross section) channels. This length scale therefore indicates the effective diameter of a circular capillary with equivalent capillary pressure.

For these example realizations, data showed an increase in pore diameter with increasing solvent fraction. This trend can be seen most clearly for $w_{MeOH} = 0.40$, where polymerizations were successful for all three solvent concentrations. As solvent fraction increases, so does total pore volume. For similar polymer globule formation characteristics (a reasonable assumption for these three cases, where porogen and monomer compositions are identical) porogenic solvents are expected to occupy volumes of larger characteristic dimension and increased pore size results.

In addition, the data of Fig. 1 suggest a maximum in d_{mode} around $w_{MeOH} = 0.5$. This is seen most clearly for $w_{solvent} = 0.70$, where mode pore diameter increased from 8.6 to 10.1 and then decreased to 9.0 µm, for $w_{MeOH} = 0.4$, 0.5, and 0.6, respectively. This result is consistent with trends observed by Yu et al. [23] who characterized the impact of porogenic solvent composition on median pore diameter. Yu reported a gradual increase in median pore diameter when increasing w_{MeOH} from 0.20 to 0.60. At $w_{MeOH} = 0.60$, pore diameter reached a maximum and then decreased suddenly upon further increase. We note that porogen composition is a particularly powerful tool for tailoring monolith pore structure for wick applications, as it has minimal impact on monolith chemical composition and porosity.

3.3. Designing high performance porous polymer wick material

We elucidate the effect of monolith microstructure on transport characteristics by again considering Darcy's Law. As Eq. (1) shows, holding all else constant, transport rate grows linearly with both permeability and liquid pressure gradient. In general, materials with large pores have high permeability, and therefore, high transport rates. At the same time, capillary transport requires small pores to maximize achievable liquid pressure gradients. In the next two sections, we will consider both permeability and capillary pressure dependency on microstructure in porous polymer monoliths. In addition, we will discuss opportunities to leverage key attributes of monolith microstructure to optimize transport for different applications.

3.3.1. Microstructure and permeability

Pore structure plays a critical role in determining resulting monolith permeability. We here discuss models for permeability, k, of Eq. (1), presented earlier. An often-used model for relating pore diameter to macroscopic permeability was developed by Carman and Kozeny [24]. Their model applies Hagen–Poiseuille type flow to an assumed pore structure comprised of many parallel, tortuous channels, of characteristic diameter, d. This results in the following relation for permeability:

$$k = \frac{\varepsilon d^2}{16k'}, \tag{2}$$

where ε is the porosity, and k' is a geometric parameter describing pore shape and tortuosity. In real systems, there is no single pore dimension, and instead, the hydraulic diameter, d_H, is typically used for characteristic diameter. d_H is defined as four times the void volume to surface area ratio. For porous media, the resulting relation is:

$$d_H = \frac{4\varepsilon}{s_o(1-\varepsilon)}, \tag{3}$$

where s_o is specific area (pore surface area normalized by solid phase volume). Substituting into Eq. (2), we see that

$$k = \frac{\varepsilon^3}{k'(1-\varepsilon)^2 s_o^2}. \tag{4}$$

When applied to packed beds of spheres, specific surface area is related to particle diameter, d_p, as $s_o = 6/d_p$. Substituting and fitting to experimental data on packed beds, Carman found $k' = 5$, and obtained the result:

$$k = \frac{\varepsilon^3 d_p^2}{180(1-\varepsilon)^2}. \tag{5}$$

Although Eq. (5) predicts permeability well for packed beds, its applicability across different types of porous media, including polymer monoliths, is limited [27]. Errors are associated with increased porosity (*i.e.*, porosity significantly greater than interstitial porosity of packed beds of spheres; typically ~0.4), wide distributions in pore diameters, and complex pore shapes and geometries. One approach is to determine an equivalent length scale describing monolith permeability, which can be used for comparison to more traditional porous media (*e.g.*, beds of packed spheres) [27]. For example, by employing Eq. (5), along with permeability measurements and an assumed packed-bed porosity of 0.4, we can determine an equivalent particle diameter, $d_{p,eq}$ [28,29]. We give calculations of such a $d_{p,eq}$ of polymer monoliths in Table 1. Although this is a useful figure of merit for comparisons of hydrodynamic performance of diverse media, the physical significance of $d_{p,eq}$ is difficult to discern, as it neither represents pore diameter nor correlates well with particle diameter, as calculated from specific surface area measurements.

Monolith pore structure complexity has limited the success of developing an analytical expression relating permeability to microscale properties. In particular, determining an appropriate length scale characterizing pore structure is difficult, as pore size distributions are often far from monodisperse. For example, Table 1 lists characteristic pore size distribution width, σ, for polymer monoliths. σ represents the standard deviation of a Gaussian, fit to the measured pore size distribution, and is an indicator of pore size variability within the monolith. As results indicate, in our polymer monoliths, distribution width is within an order of magnitude of d_{mode}.

As an approximation, Guiochon [28] suggests using a length scale related to average through-pore diameter, in conjunction

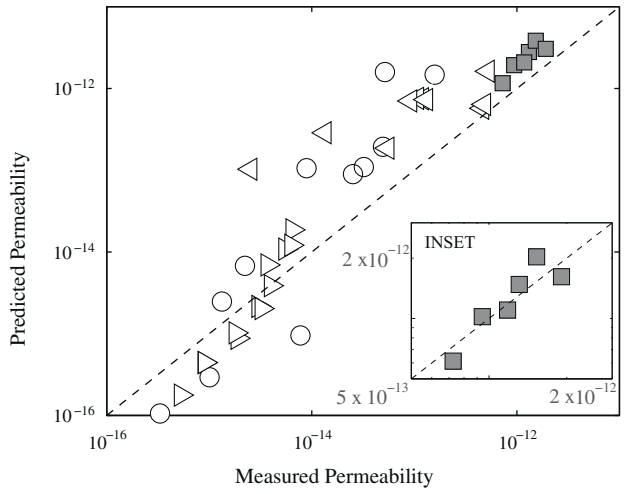

Fig. 2. Predicted versus measured permeability for polymer monoliths. Predicted permeability calculated using Eq. (2), with $d = d_{mode}$, and with $k' = 1.3$ as a fitting parameter for porous polymer monoliths. Grey symbols (■) represent monolith data from the current study as summarized in Table 1. Inset shows only the current study data for which $k' = 2.4$ provides a best fit. Open symbols represent data taken from the literature: Viklund et al. [15] (○), [30] (◁), and Merhar et al. [26] (▷). Data show rough dependence of permeability on εd_{mode}^2. Significant scatter suggests physics governing hydraulic resistance are not fully captured when using porosity and d_{mode} as a single measured length scale.

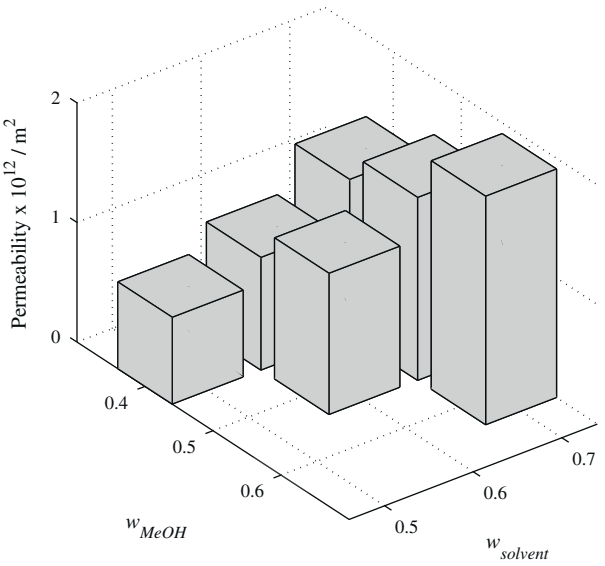

Fig. 3. Monolith permeability as a function of w_{MeOH} and $w_{solvent}$. Permeability ranged from 0.73×10^{-12} to 1.9×10^{-12} m^2. Results show permeability increased with increasing w_{MeOH} and $w_{solvent}$. Monolith permeability is consistent with trends in porosity and pore diameter (see Fig. 1).

with the Carman–Kozeny relation. Fig. 2 shows measured versus predicted permeability, when using Eq. (2) with $d = d_{mode}$ and $k' = 1.3$ for our porous samples and samples of similar structures from the literature. The published data are from three manuscripts and cover a wide range of permeabilities [26,15,30]. In addition, the inset of Fig. 2 shows measured versus predicted permeability using data from the present study only. In this inset and for these particular data, $k' = 2.4$ provided the best fit. Although results roughly show permeability dependence on εd_{mode}^2, the significant scatter in data suggests that using a single measured length may not capture key physics which arise in polymer monoliths. Although beyond the scope of this paper, further work is needed to explore specific flow effects associated with polymer monoliths, and reconcile these with porous flow data. Possible fruitful areas include accounting for bimodal pore size distributions, the topography of these complex pore networks, and effects of broad pore size distributions.

3.3.2. Permeability dependence on polymerization chemistry

In Fig. 3, we plot measured permeability of monoliths as a function of both w_{MeOH} and $w_{solvent}$. Measured permeabilities ranged from 0.73×10^{-12} to 1.9×10^{-12} m^2. Data show permeability increased with increasing MeOH and total solvent fractions. In general, results are consistent with expected dependence on monolith pore diameter and porosity. For all samples, except for HE06, mode pore diameter increased with increasing w_{MeOH} and $w_{solvent}$. In addition, porosity is approximated by $w_{solvent}$. We therefore expect increases in w_{MeOH} and $w_{solvent}$ both to contribute toward high permeability. For the current chemistry, maximum permeability was achieved for the case of maximum w_{MeOH} and $w_{solvent}$ (*i.e.*, sample HE06). This result is not expected when using d_{mode} to characterize permeability, as d_{mode} for HE06 was slightly less than for HE05. We note that d_{median}, however, was indeed greatest for HE06. These results again highlight the difficulty associated with choosing a single measured length scale to characterize monolith microstructures and predict resulting permeability. In general, however, results confirm that when designing monoliths for high permeability, chemistries which result in high porosity and large-pore diameters are desirable.

3.3.3. A note on wick geometry

We note that a wick's capacity to transport fluids is also highly dependent on macroscale wick geometry. Transport capacity increases with cross-sectional area normal to flow and is inversely proportional to characteristic wick length. For example, for the simple cylindrical shapes we fabricated for our permeability measurements (see Section 2.4), Eq. (1) can be integrated over wick cross-sectional area (normal to direction of flow), A, to obtain flow rate:

$$Q = \frac{k}{\mu}\left(\frac{A}{L}\right)\Delta P, \tag{6}$$

where L is cylinder length (along flow direction), and ΔP is the total pressure drop across the wick. For more complex geometries, Litster et al. [31] defined a shape factor of the form $(A/L)_{eff}$ which takes place of the area per length ratio in the equation above. For homogenous and isotropic wick materials (and wick dimensions significantly larger than pore dimensions) and similar flow distributions, this factor should be only a function of wick geometry and so is a key figure of merit in comparing wicks. Such formulations show how both wick microstructure (which determines k) and wick shape (which determine $(A/L)_{eff}$) are key to maximizing water transport rate.

3.3.4. Capillary transport

Capillary pressure arises due to surface tension and can be defined as the difference between gas and liquid pressures across a phase boundary. Capillary pressure is characterized by the Young-Laplace equation:

$$\Delta P = \frac{4\gamma\cos\theta}{d_{eff}}, \tag{7}$$

where γ is the surface tension, θ is the contact angle, and d_{eff} is the effective diameter of a hypothetical capillary.

An important figure of merit in wick systems is the product of the permeability of the material and the capillary pressure that it can sustain. For a given geometry (*i.e.*, for fixed A/L in Eq. (6), the maximum flow rate generated by surface tension effects is typically proportional to this product. For example, Ochterbeck [32] discusses the so-called capillary limit of heat pipes, which is defined as

when the evaporation rate exceeds the maximum capillary transport rate in the heat pipe wick. Maximum capillary transport rate in these and similar wick systems is estimated using a capillary pressure of $\Delta P_c = 4\gamma/d_{eff}$ (Young-Laplace equation, with $\theta = 0$) and fully saturated wick permeability, k. Assuming d_{eff} scales roughly with mode pore diameter,[4] we expect the maximum sustainable capillary transport rate to scale as k/d_{mode}. We therefore include this parameter on the right-hand side of Table 1.

For most applications, an ideal wick has pores small enough for sufficient capillary pressure and high permeability to minimize resistance to transport within the wick. As discussed in Section 3.3.1, permeability increases with characteristic pore diameter squared and, in most cases, capillary pressure must therefore be traded for permeability (and vice versa). Advanced wick materials, however, offer opportunity for enhanced capillary transport. For example, Huang et al. developed a micro-structured wick with a spatial gradient in pore size for use in a heat pipe. Pore size decreased from condenser to evaporator, thus simultaneously allowing for high capillary pressure in the evaporator and high permeability for transport in the adiabatic region [33]. Bimodal pore size distribution and spatial variations in microstructure that occur during polymerization [34] may possibly be leveraged for similar, high performance polymer wicks.

4. *In situ* fabrication of polymer wicks

We here describe an example application of the current porous polymer monoliths to the molding, synthesis, polymerization, and testing of *in situ* fabricated wicks for the parallel channel structure of a polymer electrolyte fuel cell cathode. We described the performance of this integrated wick and fuel cell system in a previous publication [14] but here provide new and significant details regarding polymerization, fabrication, and preparation which should be useful to other applications of these porous monoliths. Fig. 4 shows an overview of the fabrication procedure, which consists of three parts: (1 and 2) fabrication of a negative mold, (3 and 4) injection molding of polymer wicks, and (5) removal and cleaning.

4.1. Fabrication of resin negative mold

We first fabricated a resin negative mold which would later define the top surface of the final wick geometry. Steps 1 and 2 of Fig. 4 schematically show this fabrication procedure. We began with a positive template, whose geometry was precision end-milled from aluminum to match the desired top-surface geometry of the injection-molded wicks. We then transferred the positive template into a custom acrylic casting base, designed to hold the casting resin. A silicone rubber layer (not shown) between the aluminum positive template and casting base, prevented resin from seeping behind the positive template. We then coated the positive template and casting base with PVA mold-release (TAP plastics, Mountain View, CA) and allowed to dry for 1 h.

For UV initiated, *in situ* polymerization, the resin negative mold must be both UV transparent and solvent resistant. As such, we chose a polyester resin with moderate UV transparency and good solvent resistance (TAP Isophthalic High-Strength Resin, TAP Plastics, Mountain View, CA). We combined resin, catalyst (MEKP Liquid Catalyst, TAP Plastics, Mountain View, CA), and a surface curing agent (TAP Plastics, Mountain View, CA), mixed thoroughly and poured over the positive template. We allowed resin to cure at room temperature for one week. We then soaked the resin negative mold, with embedded positive template, in water to dissolve PVA mold release. We then removed the positive template, thereby leaving behind a negative image in the resin mold.

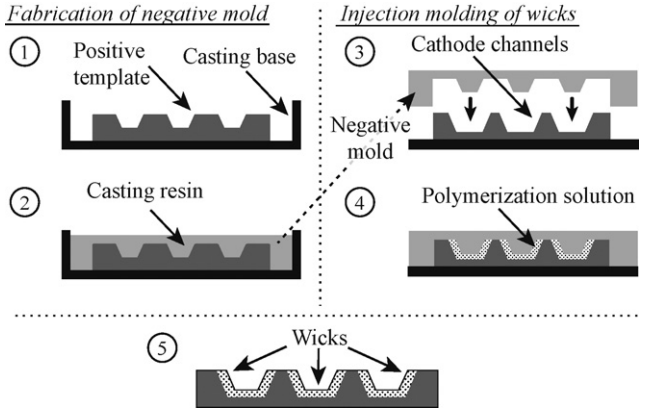

Fig. 4. Schematics of procedure for *in situ* wick fabrication. *Fabrication of negative mold*: (1) We placed an aluminum positive template into an acrylic casting base designed to hold the casting resin. This template formed one surface of the resulting wicks by defining a negative image in the resin mold, and the part of interest here (the fuel cell cathode channels) defined the opposite surface. (2) We poured a solvent-resistant polyester resin over the aluminum positive template and allowed to cure for one week. Aluminum template was then removed. *Injection molding of wicks*: (3) We sandwiched the fuel cell cathode channels between the resin negative mold and a back support plate and compressed. (4) We then injected polymerization solution to fill remaining void space (injection ports not shown and wick layer thickness exaggerated for clarity), sealed the mold assembly, and then irradiated with UV for 1 h. *Removal and cleaning*: (5) Aluminum cathode channel plate, with attached wicks, was then removed and soaked in an MeOH bath for 24 h. Sample was then dried.

4.2. Injection molding of wicks

The fuel cell cathode channels (end milled from aluminum) were roughened to improve wick adhesion, and then sandwiched between the resin negative mold and a back support plate (Fig. 4). A silicone layer between negative mold and support plate helped to seal mold assembly. The present fuel cell application required high permeability wick material. We therefore chose solution HE06 for polymerization, which we injected into the mold assembly via two leur-lock fittings (not shown), attached to the support plate. Mold assembly was then sealed and irradiated for 1 h, as described in Section 2.3 (Fig. 4, step 4).

We note that we explored both thermal and UV initiation using AIBN and benzoin methyl ether as initiators, respectively. Thermal initiation required elevated polymerization temperature (~60 °C) and long polymerization times (>12 h). Over this period, evaporative porogenic solvent loss was significant and large voids formed in the resulting wick material. UV initiation required much shorter polymerization times (<1 h) at room temperature, and evaporative losses of porogens were insignificant.

4.3. Removal and cleaning

Immediately following polymerization, we disassembled the mold assembly and carefully removed the aluminum cathode channels with polymer wicks attached (Fig. 4, step 5). We placed the newly wick-integrated cathode channels in an MeOH bath for 24 h for diffusive removal of remaining monomers and porogens, refreshing with pure MeOH every 4 h. Fig. 5 is an image of resulting cathode channels with integrated wicks. Polymerization resulted

[4] Note that the capillary pressure in a wick is a significant function of saturation, as described by Dullien [24]. Physically, this is associated with the fact that saturating liquid first fills the smallest pores associated with highest capillary pressure. Capillary pressure therefore decreases with increasing saturation. We here take the mode pore diameter simply as a scaling parameter.

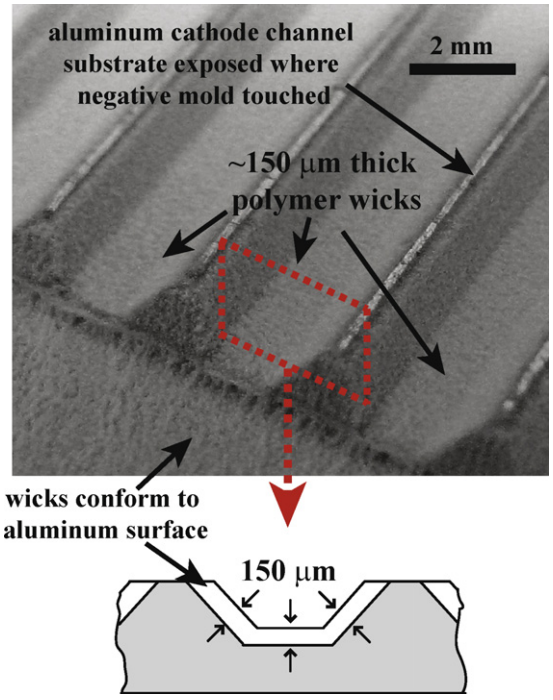

Fig. 5. Image of resulting *in situ* fabricated wick material integrated into fuel cell cathode channels. Polymerization resulted in high-quality, 150 μm thick monolithic wicks, which conform and are attached to the surface of the fuel cell cathode channels. The top of the channel-defining "ribs" are purposely left uncoated with wick material to promote good electrical contact for electrical current collection. The blow up is a cut away illustration, showing wick geometry (white) on aluminum cathode channel (grey) surface.

in high quality, monolithic, surface mounted wicks of ~150 μm thickness. This thickness is ~18 times the mean pore diameter. We note that wick thickness should be substantially greater than pore diameter to ensure good pore connectivity.

5. Conclusions and recommendations

We fabricated and characterized porous monoliths of 2-hydroxyethyl methacrylate-*co*-ethylene dimethacrylate with the aim of achieving high permeability, hydrophilic materials for use as wicks and, once saturated, water transport layers. We characterized the effect of both monomer concentration and porogenic solvent composition on resulting monolith microstructure. Our example realizations indicated mode pore diameter increased with decreasing monomer concentration and increasing mass fraction of methanol (with respect to solvents). In addition, we found monolith permeability scaled roughly with porosity times the square of mode pore diameter, and reached a maximum of 1.91×10^{-12} m^2. We recommend permeability normalized by mode pore diameter as an appropriate figure of merit which approximately captures the wick's capacity for capillary-pressure-driven flow. For a given wick geometry and flow orientation, maximum flow rate approximately scales with this figure in systems which leverage capillary pressure for liquid transport.

We then detailed a method to *in situ* polymerize wicks onto the surface of fuel cell cathode channels. Using a custom-fabricated negative mold and UV polymerization, we achieved high quality, monolithic, polymer wicks of ~150 μm thickness which conformed to the surfaces of the fuel cell cathode channels. We hypothesize that this fabrication procedure can be adapted to other applications where precisely shaped and deposited wicks are advantageous for capillary liquid and/or multiphase transport.

Recommended future directions are numerous. Presently, analytical models do not accurately predict polymer monolith permeability. As such, exploring flow effects specific to polymer monoliths, including those associated with broad and bimodal pore size distributions, may be a fruitful future research direction. In addition, unique aspects of polymer monolith microstructure, including fabrication of monoliths with macroscopic gradients in pore structure, could possibly be leveraged for high performance capillary transport. Finally, the present work represents one of many possible methods for *in situ* fabrication of polymer wicking structures. Lithographically defined wicks represent a particularly exciting potential fabrication method that may offer fine geometric control, and also be amenable to batch fabrication processes.

Acknowledgements

We gratefully acknowledge support from the National Science Foundation for a Graduate Research Fellowship for Daniel G. Strickland. We also thank Frantisek Svec for very helpful comments and suggestions, initially teaching us about *in situ* polymerization, and access to his lab at the Lawrence Berkeley National Laboratory. We also thank Raquel Ponce for help in initial prototyping efforts of porous polymer samples. The preparation of monolithic structures performed at the Molecular Foundry, Lawrence Berkeley National Laboratory, was supported by the Office of Science, Office of Basic Energy Sciences, U.S. Department of Energy, under Contract No. DE-AC02-05CH11231.

Appendix A. Supplementary data

Supplementary data associated with this article can be found, in the online version, at doi:10.1016/j.snb.2010.08.040.

References

[1] T.B. Tennikova, F. Svec, B.G. Belenkii, High-performance membrane chromatography. A novel method of protein separation, J. Liq. Chromatogr. 13 (1990) 63–70.
[2] F. Svec, Porous polymer monoliths: amazingly wide variety of techniques enabling their preparation, J. Chromatogr. A 1217 (2010) 902–924.
[3] F. Svec, J.M.J. Frechet, Continuous rods of macroporous polymer as high-performance liquid-chromatography separation media, Anal. Chem. 64 (1992) 820–822.
[4] R.E. Moore, L. Licklider, D. Schumann, T.D. Lee, A microscale electrospray interface incorporating a monolithic, poly(styrene–divinylbenzene) support for on-line liquid chromatography/tandem mass spectrometry analysis of peptides and proteins, Anal. Chem. 70 (1998) 4879–4884.
[5] X. Huang, S. Zhang, G.A. Schultz, J. Henion, Surface-alkylated polystyrene monolithic columns for peptide analysis in capillary liquid chromatography–electrospray ionization mass spectrometry, Anal. Chem. 74 (2002) 2336–2344.
[6] A. Palm, M.V. Novotny, Macroporous polyacrylamide/poly(ethylene glycol) matrixes as stationary phases in capillary electrochromatography, Anal. Chem. 69 (1997) 4499–4507.
[7] E.C. Peters, M. Petro, F. Svec, J.M.J. Frechet, Molded rigid polymer monoliths as separation media for capillary electrochromatography, Anal. Chem. 70 (1998) 2288–2295.
[8] R. Bakry, G.K. Bonn, D. Mair, F. Svec, Monolithic porous polymer layer for the separation of peptides and proteins using thin-layer chromatography coupled with MALDI-TOF-MS, Anal. Chem. 79 (2007) 486–493.
[9] A.A. Korolev, V.E. Shiryaeva, T.P. Popova, A.A. Kurganov, Fast separation of light hydrocarbons by gas chromatography on monolithic capillary columns based on silica gel, J. Anal. Chem. 62 (2007) 313–318.
[10] S. Zeng, C. Chen, J. Santiago, J. Chen, R. Zare, J. Tripp, F. Svec, J. Frechet, Electroosmotic flow pumps with polymer frits, Sens. Actuators B 82 (2002) 209–212.
[11] P.A. Levkin, S. Eeltink, T.R. Stratton, R. Brennen, K. Robotti, H. Yin, K. Killeen, F. Svec, J.M.J. Frechet, Monolithic porous polymer stationary phases in polyimide chips for the fast high-performance liquid chromatography separation of proteins and peptides, J. Chromatogr. A 1200 (2008) 55–61.
[12] T. Rohr, C. Yu, M. Davey, F. Svec, J. Frechet, Porous polymer monoliths: simple and efficient mixers prepared by direct polymerization in the channels of microfluidic chips, Electrophoresis 22 (2001) 3959–3967.
[13] F. Svec, J. Germain, J.M.J. Frechet, Nanoporous polymers for hydrogen storage, Small 5 (2009) 1098–1111.

[14] D.G. Strickland, J.G. Santiago, In situ-polymerized wicks for passive water management in proton exchange membrane fuel cells, J. Power Sources 195 (2010) 1667–1675.
[15] C. Viklund, F. Svec, J.M.J. Frechet, K. Irgum, Monolithic, "molded", porous materials with high flow characteristics for separations, catalysis, or solid-phase chemistry: control of porous properties during polymerization, Chem. Mater. 8 (1996) 744–750.
[16] J.M. Ochterbeck, Heat Transfer Handbook: Heat Pipes, John Wiley & Sons, 2003.
[17] A.W. Martinez, S.T. Phillips, G.M. Whitesides, Three-dimensional microfluidic devices fabricated in layered paper and tape, Proc. Natl. Acad. Sci. U.S.A. 105 (2008) 19606–19611.
[18] A.W. Martinez, S.T. Phillips, G.M. Whitesides, E. Carrilho, Diagnostics for the developing world: microfluidic paper-based analytical devices, Anal. Chem. 82 (2010) 3–10.
[19] S. Ge, X. Li, I. Hsing, Internally humidified polymer electrolyte fuel cells using water absorbing sponge, Electrochim. Acta 50 (2005) 1909–1916.
[20] S. Litster, C.R. Buie, T. Fabian, J.K. Eaton, J.G. Santiago, Active water management for PEM fuel cells, J. Electrochem. Soc. 154 (2007) B1049–B1058.
[21] G. Tepper, R. Kessick, Nanoelectrospray aerosols from microporous polymer wick sources, Appl. Phys. Lett. 94 (2009) 084106.
[22] V. Karola, Quartz Optical Properties, Vin Karola Instruments, 2000.
[23] C. Yu, M. Xu, F. Svec, J.M.J. Fréchet, Preparation of monolithic polymers with controlled porous properties for microfluidic chip applications using photoinitiated free-radical polymerization, J. Pol. Sci. Pol. Chem. 40 (2002) 755–769.
[24] F.A.L. Dullien, Porous Media: Fluid Transport and Pore Structure, Academic Press, 1991.
[25] E.G. Vlakh, T.B. Tennikova, Preparation of methacrylate monoliths, J. Sep. Sci. 30 (2007) 2801–2813.
[26] M. Merhar, A. Podgornik, M. Barut, M. Zigon, A. Strancar, Methacrylate monoliths prepared from various hydrophobic and hydrophilic monomers—structural and chromatographic characteristics, J. Sep. Sci. 26 (2003) 322–330.
[27] U. Tallarek, F. Leinweber, A. Seidel-Morgenstern, Fluid dynamics in monolithic adsorbents: phenomenological approach to equivalent particle dimensions, Chem. Eng. Technol. 25 (2002) 1177–1181.
[28] G. Guiochon, Monolithic columns in high-performance liquid chromatography, J. Chromatogr. A 1168 (2007) 101–168.
[29] D. Moravcova, P. Jandera, J. Urban, J. Planeta, Characterization of polymer monolithic stationary phases for capillary HPLC, J. Sep. Sci. 26 (2003) 1005–1016.
[30] C. Viklund, E. Ponten, B. Glad, K. Irgum, P. Horstedt, F. Svec, "Molded" macroporous poly(glycidyl methacrylate-co-trimethylolpropane trimethacrylate) materials with fine controlled porous properties: Preparation of monoliths using photoinitiated polymerization, Chem. Mater. 9 (1997) 463–471.
[31] S.E. Litster, C.R. Buie, J.G. Santiago, Engineering model for coupling wicks and electroosmotic pumps with proton exchange membrane fuel cells for active water management, Electrochim. Acta 54 (2009) 6223–6233.
[32] A. Bejan, A.D. Kraus, Heat pipes, in: Heat Transfer Handbook, John Wiley & Sons, 2003.
[33] X. Huang, G. Franchi, Design and fabrication of hybrid bi-modal wick structure for heat pipe application, J. Porous. Mater. 15 (2008) 635–642.
[34] H. Aoki, T. Kubo, T. Ikegami, N. Tanaka, K. Hosoya, D. Tokuda, N. Ishizuka, Preparation of glycerol dimethacrylate-based polymer monolith with unusual porous properties achieved via viscoelastic phase separation induced by monodisperse ultra high molecular weight poly(styrene) as a porogen, J. Chromatogr. A 1119 (2006) 66–79.

Biographies

Viktor Shkolnikov is a Masters candidate in mechanical engineering in Prof. Juan G. Santiago's Microfluidics Research Group at Stanford University. His work in the Stanford Microfluidics Laboratory focuses on the development of ultra thin electroosmotic micropumps for methanol delivery for PEM fuel cells. He has received his BS in Mechanical Engineering from Stanford University.

Daniel G. Strickland graduated from Stanford University with his PhD in Mechanical Engineering in June 2010. He is now assistant professor of mechanical engineering at Santa Clara University. His research is on novel water management techniques for PEM fuel cells, porous polymer-based fabrication procedures, and electrokinetic phenomena in electroosmotic pumps. He received his MS in mechanical engineering at Stanford University and BS in mechanical engineering at Seattle University. His research at Stanford University was funded through a National Science Foundation Graduate Research Fellowship.

David P. Fenning is currently a PhD student in the mechanical engineering department at the Massachusetts Institute of Technology. As part of the Laboratory for Photovoltaic Research at MIT, he studies the evolution of metal impurity defects in silicon during the thermal processing of silicon solar cells. He received his BS in mechanical engineering from Stanford University in 2008. His graduate research is supported by the National Science Foundation Graduate Research Fellowship.

Juan G. Santiago is a professor of mechanical engineering at Stanford University and Chair of the Thermosciences Group. He specializes in microscale transport phenomena and electrokinetics. He earned his PhD in mechanical engineering from the University of Illinois at Urbana-Champaign. Among other awards, he won the National Science Foundation Presidential Early Career Award for Scientists and Engineers (PECASE) ('03–'08). Santiago has presented 13 keynote and named lectures and over 100 additional invited lectures. His group has been awarded nine best paper and poster awards. He has authored/co-authored 105 archival publications, authored/co-authored 200 conference papers, and holds 24 patents.